

Modeling wheel-induced rutting in soils: Rolling

J.P. Hambleton ^a, A. Drescher ^{a,*}

^a Department of Civil Engineering, University of Minnesota, 500 Pillsbury Drive SE,
Minneapolis, MN 55455, USA

Abstract

Theoretical models for predicting penetration of non-driving (towed) rigid cylindrical wheels rolling on frictional/cohesive soils are presented. The models allow for investigating the influence of soil parameters and wheel geometry on the relationship between the inclined rolling force and wheel sinkage in the presence of permanently formed ruts. The rolling process is simulated numerically in three dimensions using the finite element code ABAQUS. The numerical simulations reveal that the advanced three-dimensional process of rutting can be regarded as steady, and an approximate analytic model for predicting sinkage under steady-state conditions, which accounts for three-dimensional effects, is also developed. The differences between wheel rolling and wheel indentation (considered in a separate paper) are discussed. Numerical and analytic results are compared with test results available in the literature and obtained from preliminary small-scale experiments, and general agreement is demonstrated.

Keywords: Rigid wheel rolling; Rutting; Finite element method; Elastic-plastic; Analytic; Experiments; PIV; Clay; Sand

Corresponding author. Tel.: +1-612-625-2374; fax: +1-612-626-7750.

E-mail addresses: dresc001@umn.edu (A. Drescher), hamb0025@umn.edu (J.P. Hambleton).

1. Introduction

Models for predicting soil rutting induced by a rolling wheel can be used to determine the impact of off-road vehicles (ORVs) in sensitive natural areas (cf. [1]), assess mobility of ORVs in adverse terrain, and facilitate methods for evaluating *in situ* soil properties premised on relating rut depth to material strength parameters [2]. Formation of permanent ruts by the rolling wheels of ORVs presents a particularly complex and challenging problem when analyzed within the framework of mechanics. The primary reason is that rutting is a result of a process rather than particular state of loading, with the latter often being sufficient in the study of geomechanics problems. When rutting occurs, the soil undergoes a loading-unloading sequence resulting from wheel contact that ultimately induces extremely large and inherently three-dimensional deformation.

In a separate paper [3], the initial phase of rutting was modeled as an indentation process in which the wheel displaces normally into the soil without rotation or horizontal (i.e., longitudinal) translation of the wheel. This paper is dedicated to modeling the formation of a rut in the process of a wheel rolling on soil and, in particular, the advanced phase when the process can be regarded as steady. In the steady configuration, stresses and the velocity field when measured with respect to the wheel do not change with time. Both papers have their origin in the exploratory work presented in [2,4] and complement numerous monographs and papers in the literature on the subject (e.g., [5-13]). All phases of rutting are considered here as quasi-static, which is acceptable for wheels traveling with slow or moderate velocities. The modeling is further limited to non-driving wheels, which do not transmit a torque. Non-driving wheels include the front wheels of many

vehicles and wheels of towed equipment. This assumption simplifies the analysis, whereas slip and erosion induced by driving wheels complicates the problem significantly.

The most essential characteristic of wheel-induced rutting is the three-dimensionality of the deformation field, which involves only one plane of symmetry parallel to the midplane of the rolling wheel. The deformation field depends on the type of soil and its previous loading history, which affect possible soil distortional and volumetric changes. Material is typically pushed in front of and to the sides of the wheel, which results in the formation of two parallel berms along an extending rut (Fig. 1a). Rigorous solutions for this complex three-dimensional problem cannot be obtained analytically, leaving numerical simulation as the only viable means for precise modeling. Valuable examples of three-dimensional numerical modeling aimed at simulating wheel penetration in soils or snow [14,15] and modeling the interaction of various tools with soils [16-18] can be found in the literature. Attempts also have been undertaken to consider rolling as a two-dimensional process [19-23].

The present paper concentrates on exploring the adequacy of modeling rutting with a simple elastic-plastic constitutive law, consisting of a linear elastic part (Young's modulus E ; Poisson's ratio ν) and perfectly-plastic part described by the Mohr-Coulomb yield condition (friction angle φ ; cohesion c) with an associated or non-associated flow rule (dilation angle $\psi \leq \varphi$). Elastic parameters play a secondary role in the analysis and were fixed at $E/\gamma d = 1000$ and $\nu = 0.3$, where wheel diameter d and soil unit weight γ are used for normalization. This elastic-plastic law was employed in preliminary analyses described in [2,4] and the detailed analysis of indentation [3] in which predicted soil

response displayed encouraging agreement with experimental data. A tacit assumption reflected in the soil constitutive models used in this paper is that the soil does not compact. Ample literature is available to show the relevance of compaction for loose materials (e.g., [24-28]), although compaction is minimal or altogether absent for a large class of materials including saturated clays and dense sands.

The main objective of the theoretical modeling presented in this paper was to arrive at a relationship between wheel load and penetration that incorporates wheel geometry and basic soil properties, considering the simplest case of a rigid, right-cylindrical wheel. Wheel sinkage, denoted s , results from both inelastic and elastic soil deformation and in general is not the same as the rut depth r , with $s \geq r$ (Fig. 1b). The difference between s and r arises due partly to elastic rebound of the soil and partly to upward plastic flow in a zone directly to the rear of the wheel, as can be seen in images of deformation induced by a rolling cylinder [7]. However, it is shown in this paper through comparison of s and r computed from numerical simulation that sinkage and rut depth can be regarded as practically interchangeable ($s \approx r$) for a non-driving wheel and the soil model considered. Since s is easily determined for a rigid wheel, being equivalent to vertical wheel displacement, it is the variable predominantly used in this paper.

As in [2-4], numerical simulations presented in this paper were performed using the explicit (dynamic) version of the computational platform ABAQUS. The numerical simulations are supplemented by an approximate analytic approach originally presented in [2,4] and expanded in [3]. The results of computations are compared with experimental data available in the literature and exploratory small-scale experiments. Finally, the similarities and differences between wheel rolling and wheel indentation are assessed.

2. Numerical simulations

The very large deformations induced by a rolling wheel make the ABAQUS/Standard (Lagrangian) version of the ABAQUS code inadequate for numerical simulations due to unacceptable distortions of the initial finite element mesh. An alternative used in this paper is the ABAQUS/Explicit version [29], which provides an arbitrary Lagrangian/Eulerian (ALE) analysis option allowing for continuous remeshing. This version also was used in [3] for analyzing wheel indentation, thus providing data for comparison that is unaffected by algorithmic differences. Use of ABAQUS/Explicit required approximating the Mohr-Coulomb yield condition by the extended Drucker-Prager yield condition [29], which may be considered a smooth counterpart of the Mohr-Coulomb criterion and has a corresponding associated or non-associated flow potential. The two conditions match exactly in stress states corresponding to triaxial compression and are in close agreement in triaxial extension.

In contrast to wheel indentation, the mesh considered in rolling consisted of two regions with different material properties. This was motivated by the fact that the formation of a rut begins when a wheel passes from a relatively strong soil onto a weak bed. To simulate this process, the soil volume was partitioned into regions of strong and weak material (Fig. 2), with material properties for the strong region consistently chosen such that little wheel penetration occurred. Both regions were discretized using 8-node linear hexahedral elements with reduced integration and hourglass control. The number of elements was roughly 65,000 in total. Out-of-plane displacements were not allowed on all boundaries except the free surface at which the wheel and soil interact, thus providing

the symmetry condition on the boundary representing the midplane of wheel (the face of the soil domain visible in Fig. 2 and parallel to the y - z plane) and giving remaining boundaries limited freedom to displace. Boundaries of the soil volume were placed far enough from the location of the wheel to have virtually no effect on the deformation field or rolling horizontal force.

The right-cylindrical wheel of diameter d and width b was modeled as an analytical rigid surface (i.e., not discretized) and governed by a single reference node located at the wheel center. The edge of the wheel was filleted, with a fillet radius of $b/20$. Introducing a fillet was necessary to avoid numerical problems in the algorithm reproducing changing contact between the rotating wheel and the soil. The soil-wheel interface was assumed to be frictional, with coefficient of friction $\mu = 0.5$.

The simulations began with application of a uniform body force over the entire soil region corresponding to the soil unit weight γ . Next, a concentrated vertical (z -direction in Fig. 2) force Q_V representative of weight on the wheel was applied gradually at the wheel reference node while the wheel was positioned on the strong soil region, and as a result the wheel settled slightly into the soil. After application of Q_V , the wheel reference node was given a horizontal (y -direction) linear velocity, which ramped up slowly to a specified value and became constant when the center of the wheel was directly above the boundary between the strong and weak soil regions. When moving horizontally, the wheel was free to rotate about its center and move vertically while the vertical force and horizontal velocity were kept constant. Wheel rotation was a result of frictional interaction at the soil-wheel contact surface. The initial vertical loading rate and

horizontal velocity were chosen small enough to guarantee negligible inertial forces, and adaptive meshing was used to avoid excessive element distortion.

During rolling, evolution of the horizontal component of the force on the wheel, denoted Q_H , and vertical wheel displacement, equivalent to sinkage s for the rigid wheel, were the particular variables of interest. Field variables in the soil region were also readily determined from the simulations, with the displacement field being of interest for comparison with experimental data. Applied vertical forces were such that computed values of steady-state sinkage were moderate (i.e., $s/d < 0.1$) and representative of those commonly encountered in application.

Pervasive numerical instabilities were encountered when attempting to simulate a wheel rolling on purely frictional soil, much like in the case of wheel indentation [3] but to a greater extent. For indentation, stability was maintained by introducing small cohesion. A similar approach was employed in the simulations of rolling, with the marked difference that the cohesion necessary for stability in the rolling case was quite large. The instabilities appear to result from the code's inability to perform calculations for stress states in the neighborhood of the yield condition's vertex, which corresponds to zero isotropic stress for cohesionless material. Unlike indentation in which isotropic stresses are primarily compressive, the deformed configuration for rolling is such that stress states are consistently near or at the yield condition's vertex, particularly at the soil surface directly to the rear of the wheel. Likewise, granular materials undergo avalanching as material collapses into the rut left by a wheel or is pushed in front of the wheel, and this phenomenon cannot be realistically reproduced by a continuum model.

3. Results of numerical simulations

Fig. 3 is an example of the deformed mesh at the end of a simulation with purely cohesive (clay) soil ($\varphi = \psi = 0$; plastic incompressibility). Normalized cohesion in the simulation was $c/\gamma d = 1.25$, and a normalized vertical force $Q_V/\gamma b d^2 = 1.9$ was applied to a wheel with aspect ratio $b/d = 0.3$. Variation of s and Q_H with horizontal wheel displacement u_y is shown in Fig. 4. As seen in this figure, sinkage and horizontal force become nearly constant after an initial transient phase of rolling (roughly $0 \leq u_y/d \leq 1.5$). This advanced phase, in which there is material upheaved in front of the wheel and a rut surrounded by two berms to the rear of the wheel (Fig. 3), can thus be regarded as steady-state operation of the wheel.

The existence of a steady state was revealed for other wheel aspect ratios, although steady state for very wide wheels (e.g., $b/d > 1.5$) and moderate to large wheel forces ($Q_V/\gamma b d^2 > 1$) was not readily achieved within the rolling distance $u_y/d \leq 2.25$ allowed by the reference configuration considered. The differing behavior for wide wheels is explained by the tendency for material to accumulate in front of the wheel rather than move to the sides. This “bulldozing” effect for wide wheels has been noted in several rolling resistance studies involving various materials [5,30,31]. Gee-Clough [31] showed a photograph of material accumulating to a height of roughly $d/2$ for a kinematically-controlled wheel ($s/d = 0.25$) with $b/d = 0.54$ operating on sand. For the sake of comparison, the maximum aspect ratio considered in this paper is $b/d = 1.2$, although such a roller geometry should be considered a cylinder, or drum, rather than a

wheel. Typical aspect ratios for wheels of SUVs, ATVs, special-purpose ORVs, and off-road motorcycles are $0.1 \leq b/d \leq 0.5$.

The results of a single three-dimensional simulation, as in Figs. 3 and 4, provide steady-state values of s and Q_H for one particular value of Q_V . Several simulations with different vertical force were thus required to obtain the global force-sinkage relationship for specified material properties and wheel geometry. The resulting steady-state force-sinkage curves for cohesive soil and some wheel aspect ratios are shown in Fig. 5. As in remaining figures, a smooth approximation to the discrete data is included to highlight trends. Clearly, the steady-state force-sinkage relationship is nonlinear, with the slope of the curves decreasing with increasing sinkage, and vertical force per unit width increases with increasing aspect ratio. Fig. 6 depicts the dependence of the force inclination angle β on s under steady-state conditions, where β is defined as (Fig. 1b)

$$\beta = \tan^{-1} \left(\frac{Q_H}{Q_V} \right) \quad (1)$$

It may be noted that plotting β as a function of s is basically equivalent to showing Q_H as a function s , with the former being a more convenient representation for the purposes of this paper. As a result of the increased accumulation in front of a relatively wide wheel, angle β increases sharply with an increase in b/d .

Steady-state force-sinkage curves resulting from simulations for a frictional soil with sufficient cohesion for computational stability ($\varphi = 30^\circ$, $\psi = 0$, $c/\gamma d = 0.25$) are shown in Fig. 7. The curves exhibit similar trends as seen for cohesive material except that force per unit width is not strictly increasing with increasing aspect ratio, being for

the most part larger with $b/d = 0.1$ than with $b/d = 0.3$. The relationship between steady-state β and s for varying b/d was found to be virtually identical to that determined for the cohesive material with $\phi = \psi = 0$ and $c/\gamma d = 1.25$ (Fig. 6). Increasing dilation angle had a similar effect on Q_V as in indentation [3], with both Q_V and β increasing substantially with increasing ψ . Also like indentation, the coefficient of interface friction $\mu > 0$ had relatively little effect on the force-sinkage curves.

In addition to sinkage, rut depth can be readily determined from numerical simulations. Fig. 8 compares sinkage and rut depth for a heavy wheel ($Q_V/\gamma b d^2 = 7$, $b/d = 0.3$) in steady rolling on various soils. It is seen that rut depth and sinkage are virtually the same when wheel penetration is significant, with elastic deformation causing some difference at small sinkage (i.e., for strong materials).

In the next section, an analytic approach for predicting steady-state wheel sinkage is developed. This method not only provides closed-form formulae but also allows for predicting sinkage on purely frictional soils.

4. Approximate analytic approach

The approximate analytic approach bears some similarity to the analysis of tillage forces considered in [32] and focuses on determining the force on a non-driving wheel in an advanced, steady state of rolling. The approach is an extension of the methodology discussed for indentation [3] and derives from preliminary work presented in [2,4]. The method hinges on two fundamental assumptions. The first is that the actual geometry of the soil-wheel contact interface can be considered equivalent to a flat rectangular surface

with area and inclination determined uniquely by the sinkage. Accordingly, the approach applies when sinkage is small relative to the wheel diameter. The second assumption is that the yielding state in the soil is such that average stress over the flat rectangular surface may be taken as the average ultimate stress (bearing capacity) for an equivalent shallow foundation. Bearing capacity is denoted q_u and calculated based on the Terzaghi-Meyerhof formula [33,34]

$$q_u = cN_c F_{cs} F_{cd} F_{ci} + qN_q F_{qs} F_{qd} F_{qi} + \frac{1}{2} \gamma B N_\gamma F_{\gamma s} F_{\gamma d} F_{\gamma i} \quad (2)$$

where $q = \gamma D$ is surcharge acting at footing depth D and B is the footing width. Formulas for the bearing capacity factors N_c, \dots, N_γ , shape factors $F_{cs}, \dots, F_{\gamma s}$, depth factors $F_{cd}, \dots, F_{\gamma d}$, and inclination factors $F_{ci}, \dots, F_{\gamma i}$ appearing in Eq. (2) are given in Appendix A.

After computing q_u according to Eq. (2), wheel force corresponding to given sinkage is determined as the product of q_u and the assumed soil-wheel contact area. The formulation is fully three-dimensional in that the shape factors in Eq. (2) account for changes in average stress arising due to the aspect ratio of the footing B/L , where $L \geq B$ is the footing length. Unlike the numerical simulations, dilation angle ψ nowhere directly enters the calculation, although the bearing capacity formula was derived semi-analytically for Mohr-Coulomb material with associated plastic flow ($\psi = \phi$).

The approximate analytic method is predicated on knowing *a priori* the force inclination angle β . This angle is related to the distribution of contact stresses over the soil-wheel interface and therefore can be assessed from experimental stress measurements [35-37]. An example of the contact stresses measured by Onafeko and

Reece [36] for a non-driving wheel is shown in Fig. 9. Based on these measurements, it is now assumed that the distribution of shear stress is antisymmetric about the ray originating from the wheel center and bisecting the arc corresponding to the soil-wheel contact interface. Likewise, it is assumed that the normal stress distribution is symmetric. From these assumptions, it follows that β is simply half of the contact angle α shown in Fig. 1b. Since α is geometrically related to s and d , angle β may be expressed as

$$\beta = \frac{\alpha}{2} = \frac{1}{2} \cos^{-1} \left(1 - 2 \frac{s}{d} \right) \quad (3)$$

Keeping only the first term of a power series expansion of β about $s/d = 0$ gives

$$\beta = \sqrt{\frac{s}{d}} \quad (4)$$

Eq. (4) is quite similar to expressions derived empirically or semi-empirically in previous works [5,31,38], in which the ratio Q_H/Q_V was expressed as simple or relatively complicated functions of $\sqrt{s/d}$.

Fig. 10 compares predicted values of β using Eq. (4) with results from numerical simulations. The equation qualitatively matches the numerical results very well, with β being somewhat underestimated with relatively large s . The numerical results predict that β depends to some extent on b/d , but agreement is reasonable for wheels of typical width. Values from numerical simulations for cohesive soil ($\varphi = \psi = 0$, $c/\gamma d = 1.25$) and frictional/cohesive soil ($\varphi = 30^\circ$, $\psi = 0$, $c/\gamma d = 0.25$) are virtually indistinguishable,

supporting the material-independence of Eq. (4). Also shown in the Fig. 10 are experimentally-determined points calculated from values of Q_V , Q_H , and s reported in [36], which agree very well with predictions from Eq. (4).

Two versions of the analytic approach, which handle the effects of inclined loading in different ways, are now considered.

4.1 Inclined force method

In the first version of the analytic approach, the wheel is effectively replaced by a horizontal footing, and the total force Q is therefore inclined relative to the footing (Fig. 11c). This formulation, referred to as the “inclined force method,” therefore accounts for the effect of inclination directly through the inclination factors $F_{ci}, \dots, F_{\gamma i}$ appearing in Eq. (2). In keeping with considering the footing to be horizontal, the footing contact distance h is taken as shown in Fig. 11a and is geometrically related to sinkage and wheel diameter as

$$h = \sqrt{ds - s^2} \tag{5}$$

The footing width B and length L in the bearing capacity formula are then

$$\left. \begin{array}{l} B = h \\ L = b \end{array} \right\} \text{for } h < b, \quad \left. \begin{array}{l} B = b \\ L = h \end{array} \right\} \text{for } h \geq b \tag{6}$$

and the total force Q together with its vertical component Q_V are

$$Q = q_u bh, \quad Q_V = Q \cos \beta = q_u bh \cos \beta \quad (7)$$

The variable D appearing in (2) is viewed as accounting for material pushed in front and along the sides of the wheel, and it enters through the surcharge $q = \gamma D$ and the depth factors $F_{cd}, \dots, F_{\gamma d}$. Depth D is estimated by considering mass balance of soil displaced by the wheel [2], resulting in the approximation

$$D = \frac{1}{6} s \quad (8)$$

Final algebraic expressions relating Q_V to s , b , d , ϕ , c , and γ are determined by substituting results (2), (4)-(6), and (8) into Eq. (7). The resulting equations are in Appendix A.

4.2 Inclined footing method

A second version of the analytic method is developed by replacing the wheel with an equivalent footing that is inclined at angle β to the horizontal (Fig. 11d). This version is referred to as the “inclined footing method.” With the footing inclined at angle β , the total force Q is necessarily perpendicular to the footing, and the configuration is nearly identical to the case of a vertically loaded footing on a slope. Bearing capacity for a footing on sloping ground can be calculated with formula (2) using modified bearing

capacity factors N_c^* , N_q^* , and N_γ^* . The modified factors proposed in [39,40], given in Appendix A, are used in further developments. An error is introduced because the modified bearing capacity factors were derived for gravity acting perpendicular to the footing, although this error is minimal for small sinkage. Also, shape and depth factors are taken to be the same as for a footing on horizontal ground, despite the fact that they are somewhat different for sloping ground.

In addition to the modified bearing capacity factors, the inclined footing method differs in how the footing length and equivalent depth D are calculated. The variable h in the inclined force method is replaced with h^* (Fig. 11a), where

$$h^* = \sqrt{ds} \quad (9)$$

Depth D is also replaced with D^* to be consistent with the concept of a footing on sloping ground:

$$D^* = D \cos \beta = \frac{1}{6} s \cos \beta \quad (10)$$

The final force-sinkage equations resulting from the inclined footing method are in Appendix A.

5. Results of approximate analytic approach

Force-sinkage curves predicted using the analytic approach are similar in character to the numerical results. Fig. 12 shows example curves using the inclined footing method for varying soil properties and $b/d = 0.2$. Sinkage at which $B = L$ is clearly visible in the figure, as the first derivative of Q_V with respect to s is discontinuous at this point. As with the curves from numerical simulation, vertical force is a nonlinear function of sinkage, with the force increasing at a decreasing rate. For cohesive soil ($\varphi = 0$), force increases roughly linearly with cohesion, and for frictional soil ($c = 0$), force increases almost exponentially with friction angle.

Fig. 13 compares results from numerical simulation with those from the analytic approach for cohesive soil. The inclined footing method gives curves situated above those from the inclined force method, and they locate closer to curves obtained from numerical simulations. The analytic approach qualitatively predicts the same dependence of force on the wheel aspect ratio (i.e., three-dimensional effects) as the numerical simulations. The overall shape of the curves resulting analytically and numerically is similar, with better agreement at small sinkage than large sinkage.

Fig. 14 compares analytic and numerical results for frictional/cohesive soil. Trends are similar to the case of cohesive soil, and the inclined footing method again gives predictions closer to numerical simulations than the inclined force method. Agreement between analytic and numerical predictions for $b/d = 0.3$ is quantitatively quite good, whereas the discrepancy is considerable for $b/d = 0.1$. Furthermore, the analytic approach and numerical simulations contradict one another in terms of how force

is affected by b/d at relatively large sinkage, with numerical simulations indicating that force per unit width should be higher for $b/d = 0.1$ than $b/d = 0.3$ and the analytic approach predicting the opposite. The analytic approach does, however, predict the same trend as the numerical simulations in the interval $0 \leq s/d \leq 0.025$. Effects of b/d in the analytic method are linked to the shape factors present in the bearing capacity formula (Eq. (2)), and differences with numerical results point to possible improvements to these factors (e.g., [41]).

6. Experiments

Simple constitutive models for the soil were used in the numerical and approximate analytic approaches presented in previous sections. To assess the capability of both approaches in predicting wheel sinkage in real soils, limited experimental data were generated using two setups similar to those used for indentation [3]. The first setup, consisting of a 780mm \times 440 mm \times 80 mm container with a Plexiglas front wall, provided information on the incremental displacement field in a granular material subject to wheel rolling. The material consisted of crushed walnut shells, characterized in [3, 42], over which an acrylic wheel of diameter $d = 100$ mm and width $b = 19$ mm was rolled next to the transparent wall to simulate one-half of a three-dimensional rolling wheel with $b/d = 0.38$. The wheel was attached to a horizontal shaft and rolled at prescribed sinkage (kinematic control), meaning that the wheel's axis of rotation was kept at the same position relative to the undisturbed material surface as the wheel moved. The wheel was free to rotate (i.e., non-driving or towed wheel), with free rotation facilitated by leaving a

very small gap between the wheel and Plexiglas wall. Even though the friction between the material and wall affected local displacements, it may be argued that the measurements represent quantities at the midplane of a fully three-dimensional configuration reasonably well.

Figure 15a is an example of the displacement increment field obtained using digital photography processed using particle image velocimetry (PIV) software [43]. Prescribed sinkage was $s/d = 0.04$, with analysis of the deformation at several wheel locations indicating a nearly steady field. Accumulation in region $BCDKB$ is clearly visible, and because the wheel is transparent, the height of material flowing to the side of the wheel and forming a berm can be seen. Particles move forward within zone $ABCDEIJA$ in front of the wheel, and particles move rearward in region $EFGHI$ below and to the rear of the wheel. Regions $ABJA$ and $EGHE$ are characterized by upward motion, and particles move downward in zone $DEID$. Regions $DIJD$ and $EHIE$ are transition regions with both downward and upward flow. Overall, the mechanism looks like a skewed version of the classical Prandtl failure mechanism for a shallow footing [44], with the key difference that no distinct boundaries with a jump in displacement increments (shear bands [45] or shocks [46]) were observed. Vectors are not shown in regions $BCDKB$ and $EFLE$ due to poor image correlation in the PIV analysis, which appears to be the result of avalanching and particle rotation in these regions.

In view of failed numerical simulations of rolling on purely frictional material, no direct comparison with experiments was possible. Instead, a simulation of rolling on a frictional/cohesive material with $\phi = 40^\circ$, $\psi = 20^\circ$, and $c/\gamma d = 20$ is shown in Fig. 15b. The friction and dilation angles are roughly the measured properties for the material and gave

numerical results agreeing favorably with the experimentally-determined kinematics for indentation [3]. It is evident that in spite of large cohesion the field of displacement increments resembles the experimental one, and this is consistent with the generally-accepted observation from numerous geomechanics problems (e.g., retaining walls and foundations) that cohesion does not affect the kinematics significantly in the region of induced shear.

Several features in the experiment are not, however, reproduced in the numerical simulation. Namely, numerical results show no rearward flow zone and give that the height of material pushed in front of the wheel is approximately 1.5 times that measured experimentally. These differences appear to be caused by the cohesion required for computational stability. It is not surprising that a discrepancy arises in the zone directly below and to the rear of the wheel, as it is this region where tensile isotropic stresses develop in the numerical simulation despite the fact that such stresses cannot exist in granular material. Similarly, avalanching of material in front of the wheel was observed in the experiments but does not occur in the simulation, with avalanching causing the height of material in front of the wheel to decrease.

The second experimental setup was aimed at providing data on the relationship between the vertical force on the rolling wheel and sinkage in a true three-dimensional setting. These were conducted on saturated clay and dry sand (described in [3]) placed in a 100 mm \times 250 mm \times 300 mm container. The container was affixed to a linear bearing, and a wheel of diameter $d = 115$ mm and width $b = 38$ mm with coarse sandpaper adhered to the contacting surface was attached to a load cell connected to a vertical shaft above the center of the container. The load cell was oriented to measure the vertical

component of force acting on the wheel, and it was verified that horizontal force on the wheel, which was not measured during the experiments, had an insignificant affect on readings of vertical force. As with the experiment involving PIV, the wheel was free to rotate, such that a non-driving wheel was replicated. The wheel was lowered to prescribed sinkage, and the container was then moved horizontally by means of a stepper motor. After initial variation, the vertical force became nearly constant with further rolling of the wheel, thus indicating a state close to being steady. Several tests with different sinkage were conducted to construct the force-sinkage curves.

Experimental results are shown in Fig. 16 together with superimposed curves obtained from numerical simulations and the analytic approach using ϕ and c (as well as E in numerical simulation) as determined from uniaxial and triaxial compression [3]. The theoretical predictions agree favorably with the experimental results, particularly for the sand. For the clay, both numerical and analytic predictions somewhat overestimate the wheel force at small sinkage, and the analytic method somewhat underestimates the force at large sinkage. As results using the analytic approach are based on the inclined footing method, it appears that the inclined footing method provides more realistic predictions than the inclined force method.

Predictions using the analytic approach are also compared with force-sinkage data obtained by Willis et al. [47], who performed tests with rigid wheels on clay and sand. The test procedure consisted of rolling a wheel under given vertical load (static control) and measuring sinkage. Reported properties were $\phi = 7^\circ$ and $c = 22$ kPa for the clay. Properties for the sand were $\phi = 35^\circ$ and $\gamma = 14$ kN/m³. It is not clear from the text how ϕ and c were determined by the authors, but the values are nevertheless typical for clay

with high water content and medium density sand. Comparison is made with test results for a wheel with $d = 406$ mm and $b = 76$ mm on clay and a wheel with $d = 406$ mm and $b = 114$ mm on sand. The experimental data are shown in Fig. 17 and compared with theoretical predictions using the analytic method. Very good agreement is seen in the comparison for clay, and reasonable agreement is found for sand. Commensurate with the uncertainty in measured soil properties, two theoretical curves are presented for the sand, which also show the sensitivity of the prediction with respect to ϕ .

7. Comparison between rolling and indentation

Fig. 18a shows, based on numerical simulation with cohesive soil, the relationship between vertical force and steady-state sinkage for rolling as compared with indentation [3]. Qualitatively, the shape of the curves is very similar; however, the magnitude of the force for a given sinkage in rolling is just over half of that for indentation. As no numerical results were available for purely frictional material, only the approximate analytic results are compared (Fig. 18b). At given sinkage, vertical force for rolling is drastically less than with indentation. These differences between rolling and indentation for cohesive and frictional soils are further supported by the experimental results shown in Fig. 19. Obviously, there is a fundamental difference in the deformation field in rolling and indentation, and therefore no direct comparison is made.

There are three essential differences between indentation and rolling of a non-driving wheel. The first basic difference is that the soil-wheel contact area in the rolling process is smaller than with indentation at the same sinkage. This area in rolling is

approximately half of that in indentation, and this is clearly seen in the expressions used in the analytic approach for the contact length h with rolling (Eqs. (5) and (9))

$$h = \sqrt{ds - s^2} \approx h^* = \sqrt{ds} \quad (\text{small } s/d) \quad (11)$$

and with indentation [3]

$$h = 2\sqrt{ds - s^2} \quad (12)$$

If one regards vertical force as being fixed, the contact area reduction in rolling as compared to indentation requires that the wheel sinks deeper during rolling. The second key difference is that the load is inclined in rolling, which also causes a rolling wheel to sink more than an indenting wheel with the same vertical force. Lastly, rolling and indentation are distinguished by the tendency for material to accumulate in front of a rolling wheel. The significance of accumulation can be shown by comparing the effects of the wheel aspect ratio for rolling and indentation with cohesive material. In rolling, vertical force per unit width was found to be strictly increasing with increasing b/d (Fig. 5). In indentation [3], vertical force per unit width for given sinkage was found to be relatively insensitive to b/d . The change in dependence on b/d between rolling in indentation is explained by resistance from accumulated material in front of the wheel during the rolling process.

8. Closing remarks

In numerical simulations, success in reproducing three-dimensional deformation fields around a non-driving wheel strongly depended on the value of the friction angle and cohesion. For cohesive soil ($\phi = \psi = 0$), the solutions were numerically stable. Simulations of rolling on a purely frictional ($c = 0$) material failed, and this illustrates the limitations of the particular code and soil constitutive model chosen. This failure can be attributed to very large deformations induced by a rolling wheel and corresponding near-zero isotropic stresses over a significant portion of the material deforming around the wheel. Adding significant cohesion moves the vertex in the yield condition and flow potential into the tensile zone away from zero isotropic stresses, lends stability to the simulations, and prohibits material avalanching in regions ahead of and to the rear of the wheel where it is prone to occur. Effects of dilatancy were not explicitly presented for rolling but were found to be virtually the same as in indentation [3], with an increase in dilation angle having a significant influence on vertical and horizontal forces at a given sinkage.

Overall, the numerical and analytic approaches predict similar trends in the force-sinkage curves for a rolling wheel, with vertical force increasing with sinkage at decreasing rate. Quantitative agreement between the numerical and analytic curves is also reasonable. The theoretical predictions match the results of small-scale experiments very well, and supplemental data from the literature [47] support this conclusion. Roughly speaking, sinkage is inversely proportional to the width of the wheel for sandy soils and inversely proportional to the width squared for cohesive soils. Thus, reducing wheel

width by half leads to a two-fold increase in sinkage with sands and to a four-fold increase in sinkage with clays. For both types of soil, sinkage is nearly inversely proportional to wheel diameter, which implies for fixed wheel force a two-fold increase in sinkage with either soil when wheel diameter is reduced by half.

Even though stable numerical simulations required significant cohesion, it appears that the occurrence of localized deformation (shear bands or shocks) observed in many classical geomechanics problems (retaining walls, slopes, foundations) does not take place in wheel rolling. The lack of localized deformation also was observed in the small-scale experiments on granular material. Geomechanics problems are often solved or tested as two-dimensional (plane strain) problems, while the simulations and experiments presented in this paper are three-dimensional. It is known (cf. [45]) that plane strain problems are susceptible to deformation localization, particularly for non-associated flow rules, whose adequacy has been generally accepted in view of tests on specimens of frictional soils.

In presenting the results, attention was focused on the vertical component of wheel force, as it equals weight on the wheel and appears to be the most important contributor to rutting caused by non-driving wheels. Horizontal (i.e., longitudinal) component of force was also determined, although this force is of interest in studying vehicle mobility and falls outside the scope of this paper.

The results above indicate the ability of the simplified constitutive models to reproduce, approximately at least, the relationship between the force on a rolling wheel and wheel sinkage for different soils and moderate sinkage ($s/d < 0.1$). Predictions closer to experimental data would require more sophisticated soil models. As the emphasis was

on the influence of plastic parameters, a limited set of representative elastic parameters was used in the simulations. The numerical simulations also showed (and the analytic solutions assume) the existence of a rut and berms left by a rolling wheel. As the volume of berms compensating volumetrically for material missing in the rut is small, it may be difficult to assess as whether modeling rut formation necessarily requires a constitutive model allowing for compaction or not. Indeed, it was noted in tests on saturated (nearly incompressible) clay that the material outside the rut was elevated by a hardly discernable amount and spread over a relatively large area. This was also observed in the numerical simulations of these experiments. Certainly, in very loose soils or snow, disregarding compaction is unacceptable.

Several conclusions obtained from the analysis of a non-driving wheel closely match those obtained from modeling wheel indentation [3]. Force-sinkage curves have similar shape, and the deformation field is unquestionably three-dimensional in both. Lack of localized deformation was also observed in both processes. Of particular interest in detecting weak soils is the observation that the vertical force in rolling is a predictable fraction, dependent on material properties, of that in indentation. This may provide a practical, first order link between continuous rolling processes and the local penetration process.

Acknowledgements

Financial support provided by the Minnesota Local Road Research Board and the Shimizu Corporation are gratefully acknowledged. Computer resources were provided by the Minnesota Supercomputing Institute.

Appendix A

Bearing capacity factors [44,48,49]:

$$N_q = \tan^2 \left(\frac{\pi}{4} + \frac{\varphi}{2} \right) e^{\pi \tan \varphi}, \quad N_c = (N_q - 1) \cot \varphi, \quad N_\gamma = 2(N_q + 1) \tan \varphi$$

Shape factors [50]:

$$F_{cs} = 1 + \frac{B}{L} \frac{N_q}{N_c}, \quad F_{qs} = 1 + \frac{B}{L} \tan \varphi, \quad F_{\gamma s} = 1 - 0.4 \frac{B}{L}$$

Depth factors ($D/B \leq 1$) [40]:

$$F_{cd} = 1 + 0.4 \frac{D}{B}, \quad F_{qd} = 1 + 2 \tan \varphi (1 - \sin \varphi)^2 \frac{D}{B}, \quad F_{\gamma d} = 1$$

Inclination factors [34]:

$$F_{ci} = F_{qi} = \left(1 - \frac{\beta^\circ}{90^\circ} \right)^2, \quad F_{\gamma i} = \left(1 - \frac{\beta}{\varphi} \right)^2$$

Modified bearing capacity factors [39,40]:

$$N_c^* = \cot \varphi \left(e^{-2\beta \tan \varphi} N_q - 1 \right), \quad N_q^* = N_q (1 - \tan \beta)^2, \quad N_\gamma^* = N_\gamma (1 - \tan \beta)^2$$

Analytic approach; inclined force method:

$$\begin{aligned}
Q_v = & b\sqrt{ds-s^2} \cos\left(\sqrt{\frac{s}{d}}\right) \left\{ cN_c \left(1 + \frac{\sqrt{ds-s^2}}{b} \frac{N_q}{N_c} \right) \left[1 + 0.07 \frac{s}{\sqrt{ds-s^2}} \right] \left(1 - 0.64 \sqrt{\frac{s}{d}} \right)^2 \right. \\
& + 0.17\gamma s N_q \left(1 + \frac{\sqrt{ds-s^2}}{b} \tan \phi \right) \left[1 + 0.33 \tan \phi (1 - \sin \phi)^2 \frac{s}{\sqrt{ds-s^2}} \right] \\
& \left. \times \left(1 - 0.64 \sqrt{\frac{s}{d}} \right)^2 + \gamma \sqrt{ds-s^2} N_\gamma \left(0.5 - 0.2 \frac{\sqrt{ds-s^2}}{b} \right) \left(1 - \frac{1}{\phi} \sqrt{\frac{s}{d}} \right)^2 \right\}
\end{aligned}$$

for $\sqrt{ds-s^2} < b$

$$\begin{aligned}
Q_v = & b\sqrt{ds-s^2} \cos\left(\sqrt{\frac{s}{d}}\right) \left\{ cN_c \left(1 + \frac{b}{\sqrt{ds-s^2}} \frac{N_q}{N_c} \right) \left[1 + 0.07 \frac{s}{b} \right] \left(1 - 0.64 \sqrt{\frac{s}{d}} \right)^2 \right. \\
& + 0.17\gamma s N_q \left(1 + \frac{b}{\sqrt{ds-s^2}} \tan \phi \right) \left[1 + 0.33 \tan \phi (1 - \sin \phi)^2 \frac{s}{b} \right] \\
& \left. \times \left(1 - 0.64 \sqrt{\frac{s}{d}} \right)^2 + \gamma b N_\gamma \left(0.5 - 0.2 \frac{b}{\sqrt{ds-s^2}} \right) \left(1 - \frac{1}{\phi} \sqrt{\frac{s}{d}} \right)^2 \right\}
\end{aligned}$$

for $\sqrt{ds-s^2} \geq b$

Analytic approach; inclined footing method:

$$\begin{aligned}
Q_v = & b\sqrt{ds} \cos\left(\sqrt{\frac{s}{d}}\right) \left\{ cN_c \left(1 + \frac{\sqrt{ds}}{b} \frac{N_q}{N_c} \right) \left(1 + 0.07 \frac{s}{\sqrt{ds}} \cos\left(\sqrt{\frac{s}{d}}\right) \right) \left(\frac{N_q e^{-2\sqrt{\frac{s}{d}} \tan \phi} - 1}{N_q - 1} \right) \right. \\
& + \left[0.17\gamma s N_q \cos\left(\sqrt{\frac{s}{d}}\right) \left(1 + \frac{\sqrt{ds}}{b} \tan \phi \right) \left(1 + 0.33 \tan \phi (1 - \sin \phi)^2 \cos\left(\sqrt{\frac{s}{d}}\right) \frac{s}{\sqrt{ds}} \right) \right. \\
& \left. \left. + \gamma \sqrt{ds} N_\gamma \left(0.5 - 0.2 \frac{\sqrt{ds}}{b} \right) \right] \left[1 - \tan\left(\sqrt{\frac{s}{d}}\right) \right]^2 \right\}
\end{aligned}$$

for $\sqrt{ds} < b$ and

$$\begin{aligned}
Q_v = & b\sqrt{ds} \left\{ cN_c \left(1 + \frac{b}{\sqrt{ds}} \frac{N_q}{N_c} \right) \left(1 + 0.07 \frac{s}{b} \cos \left(\sqrt{\frac{s}{d}} \right) \right) \left(\frac{N_q e^{-2\sqrt{\frac{s}{d}} \tan \phi} - 1}{N_q - 1} \right) \right. \\
& + \left[0.17 \gamma s N_q \cos \left(\sqrt{\frac{s}{d}} \right) \left(1 + \frac{b}{\sqrt{ds}} \tan \phi \right) \left(1 + 0.33 \tan \phi (1 - \sin \phi)^2 \cos \left(\sqrt{\frac{s}{d}} \right) \frac{s}{b} \right) \right. \\
& \left. \left. + \gamma b N_\gamma \left(0.5 - 0.2 \frac{b}{\sqrt{ds}} \right) \right] \left[1 - \tan \left(\sqrt{\frac{s}{d}} \right) \right]^2 \right\}
\end{aligned}$$

for $\sqrt{ds} \geq b$.

References

- [1] Li Q, Ayers PD, Anderson, AB. Prediction of impacts of wheeled vehicles on terrain. *J Terramech* 2007;44(2):205-215.
- [2] Hambleton JP. Modeling test rolling in clay. MS thesis, University of Minnesota, Minneapolis; 2006.
- [3] Hambleton JP, Drescher A. Modeling wheel-induced rutting in soils: Indentation. *J Terramech* 2008 (in press).
- [4] Hambleton JP, Drescher A. Modeling test rolling on cohesive subgrades. In: Proc. of the int. conf. on advanced characterisation of pavement and soil engineering materials, vol. 1. Athens, Greece, June 2007:359-368.
- [5] Bekker MG. Introduction to terrain-vehicle systems. Ann Arbor: University of Michigan Press; 1969.
- [6] Karafiath LL, Nowatzki EA. Soil mechanics for off-road vehicle engineering, Clausthal: Trans Tech Publications; 1978.
- [7] Wong JY. Theory of ground vehicles. New York: Wiley; 2001.
- [8] McRae JL. Theory for a towed wheel in soil. *J Terramech* 1964;1(4):31-53.
- [9] Maclaurin EB. Soil-vehicle interaction. *J Terramech* 1987;24(4):281-294.
- [10] Gee-Clough, D. Soil-vehicle interaction (B). *J Terramech* 1991;28(4):289-296.
- [11] Muro T. Braking performances of a towed rigid wheel on a soft ground based on the analysis of soil-compaction. *Soils Found* 1993;33(2):91-104.

- [12] Shibly H, Iagnemma K, Dubowsky S. An equivalent soil mechanics formulation for rigid wheels in deformable terrain, with application to planetary exploration rovers. *J Terramech* 2005;42(1):1-13.
- [13] Maciejewski J, Jarzebowski A. Experimental analysis of soil deformation below a rolling rigid cylinder. *J Terramech* 2004;41(4):223-241.
- [14] Chiroux RC, Foster WA, Johnson CE, Shoop SA, Raper RL. Three-dimensional finite element analysis of soil interaction with a rigid wheel. *Appl Math and Comp* 2005;162(2):707-722.
- [15] Shoop SA, Haehnel R, Kestler K, Stebbings K, Alger R. Finite element analysis of a wheel rolling in snow. In: *Proc. of the 10th int. conf. on cold regions engineering*. Lincoln, NH, USA, August 1999:519-30.
- [16] Abo-Elnor M, Hamilton R, Boyle JT. 3D Dynamic analysis of soil-tool interaction using the finite element method. *J Terramech* 2003;40(1):51-62.
- [17] Karmakar S, Kushwaha RL. Dynamic modeling of soil-tool interaction: An overview from a fluid flow perspective. *J Terramech* 2006;43(4):411-425.
- [18] Plouffe C, Laguë C, Tessier S, Richard MJ, McLaughlin NB. Moldboard plow performance in a clay soil: Simulations and experiment. *Trans ASAE* 1999;42(6):1531-1539.
- [19] Yong RN, Fattah EA, Boonsinsuk P. Analysis and prediction of tyre-soil interaction and performance using finite elements. *J Terramech* 1978;15(1):43-63.
- [20] Block, WA, Johnson CE, Bailey AC, Burt EC, Raper RL. Energy analysis of finite element soil stress prediction. *Trans ASAE* 1994;37(6):1757-1762.
- [21] Foster WA, Johnson CE, Raper RL, Shoop SA. Soil deformation and stress analysis under a rolling wheel. In: *Proc. of the 5th North American ISTVS conference/workshop*. Saskatoon, SK, Canada, May 1995:194-203.
- [22] Liu CH, Wong JY. Numerical simulations of tire-soil interaction based on critical state soil mechanics. *J Terramech* 1996;33(5):209-221.
- [23] Fervers CW. Improved FEM simulation model for tire-soil interaction. *J Terramech* 2004;41(2-3):87-100.
- [24] Adebisi OA, Koike M, Konaka T, Yuzawa S, Kuroishi I. Compaction characteristics for the towed and driven conditions of a wheel operating in an agricultural soil. *J Terramech* 1991;28(4):371-382.

- [25] Chi L, Tessier S, Laguë C. Finite element prediction of soil compaction induced by various running gears. *Trans ASAE* 1993;36(3):629-636.
- [26] Arvidsson J, Ristic S. Soil stress and compaction effects for four tractor tyres. *J Terramech* 1996;33(5):223-232.
- [27] Muro T, He T, Miyoshi M. Effects of a roller and a tracked vehicle on the compaction of a high lifted decomposed granite sandy soil. *J Terramech* 1998;35(4):265-293.
- [28] Botta GF, Jorajuria D, Draghi LM. Influence of axle load, tyre size and configuration on the compaction of a freshly tilled clay. *J Terramech* 2002;39(1):47-54.
- [29] ABAQUS Version 6.6 Documentation. Providence: ABAQUS, Inc.; 2004.
- [30] Sitkei G. The bulldozing resistance of towed wheels in loose sand. *J Terramech* 1966;3(2):25-37.
- [31] Gee-Clough D. The effect of wheel width on the rolling resistance of rigid wheels in sand. *J Terramech* 1979;15(4):161-184.
- [32] Godwin RJ, O'Dogherty MJ. Integrated soil tillage force prediction models. *J Terramech* 2007;44(1):3-14.
- [33] Terzaghi K. *Theoretical soil mechanics*. New York: Wiley; 1943.
- [34] Meyerhof GG. Some recent research on bearing capacity of foundations. *Can Geotech J* 1963;1(1):16-26.
- [35] Uffelmann FL. The performance of rigid cylindrical wheels on clay soil. In: *Proc. of the 1st int. conf. on the mechanics of soil-vehicle systems*. Torino, Italy, April 1961.
- [36] Onafeko O, Reece AR. Soil stresses and deformations beneath rigid wheels. *J Terramech* 1967;4(1):59-80.
- [37] Krick G. Radial and shear stress distribution under rigid wheels and pneumatic tires operating on yielding soils with consideration of tire deformation. *J Terramech* 1969;6(3):73-98.
- [38] McRae JL. Theory for a towed wheel in soil. *J Terremech* 1964;1(4):31-53.
- [39] Chen WF. *Limit analysis and soil plasticity*. Amsterdam: Elsevier; 1975.

- [40] Hansen JB. A revised and extended formula for bearing capacity. Bulletin 28. Copenhagen: Danish Geotechnical Institute; 1970.
- [41] Zhu M, Michalowski RL. Shape factors for limit loads on square and rectangular footings. *J Geotech Geoenviron Eng* 2005;131(2):223-231.
- [42] Waters AJ, Drescher A. Modeling plug flow in bins/hoppers. *Powd Techn* 2000;113(1):168-175.
- [43] White DJ, Take WA, Bolton MD. Soil deformation measurement using particle image velocimetry (PIV) and photogrammetry. *Geotechnique* 2003;53(7):619-731.
- [44] Prandtl L. Über die Eindringungsfestigkeit (Härte) plastischer Baustoffe und die Festigkeit von Schneiden. *Zeit angew Math Mech* 1921;1(1):15-20.
- [45] Vardoulakis I, Sulem J. Bifurcation analysis in geomechanics. London: Chapman and Hall; 1995.
- [46] Drescher A, Michalowski RL. Density variation in pseudo-steady plastic flow of granular media. *Geotechnique* 1984;34(1):1-10.
- [47] Willis BMD, Barret FM, Shaw GJ. An investigation into rolling resistance theories for towed rigid wheels. *J Terramech* 1965;2(1):24-53.
- [48] Reissner H. Zum Erddruckproblem. In: Proc. of the 1st int. congress for applied mechanics. Delft, The Netherlands 1924:295-311.
- [49] Vesic AS. Analysis of ultimate loads of shallow foundations. *J Soil Mech Found Div ASCE* 1970;99(1):45-73.
- [50] De Beer EE. Experimental determination of the shape factors and bearing capacity factors of sand. *Geotechnique* 1970;20(4):387-411.

Figures

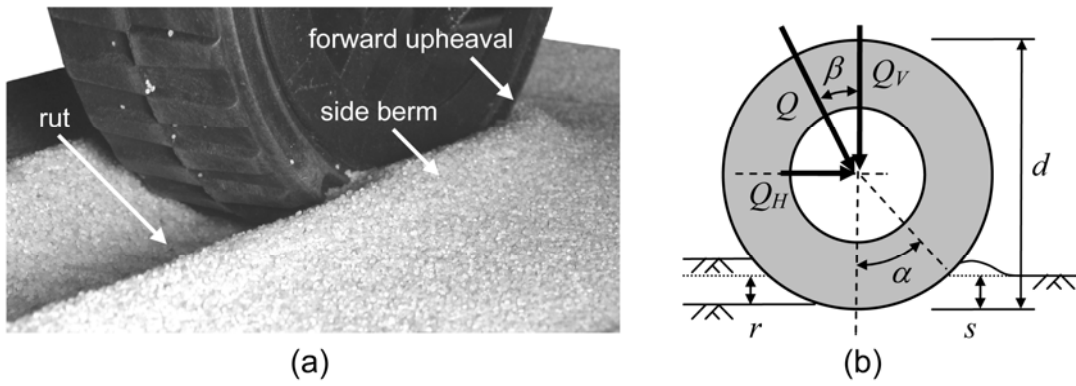


Fig. 1. Deformation induced by non-driving wheel: (a) photograph of wheel on medium density sand; (b) schematic depicting sinkage, rut depth, and wheel forces.

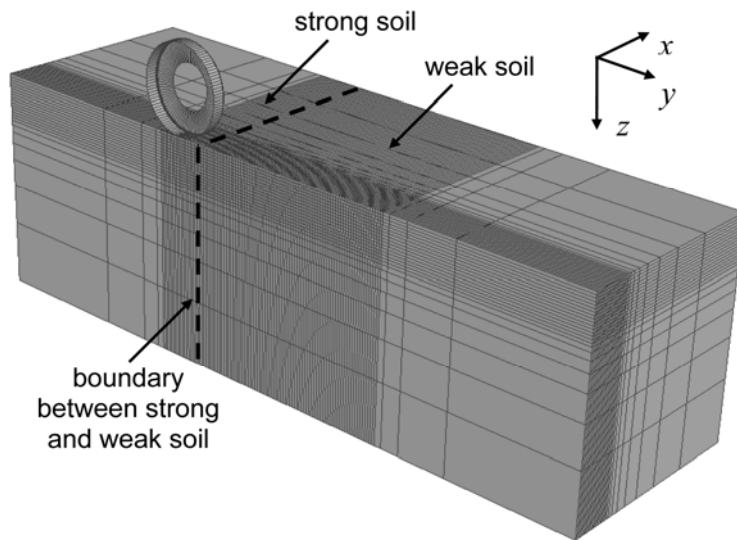


Fig. 2. Reference configuration for numerical simulation of rolling wheel (wheel travels in positive y -direction).

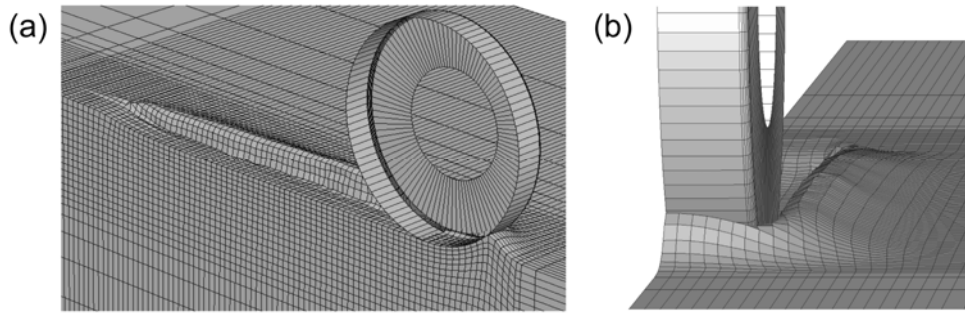


Fig. 3. Deformed mesh at end of simulation with cohesive soil ($\varphi = \psi = 0$, $c/\gamma d = 1.25$, $b/d = 0.3$, $Q_V/\gamma b d^2 = 1.9$): (a) side view (direction of wheel travel is from left to right); (b) view from in front of the wheel.

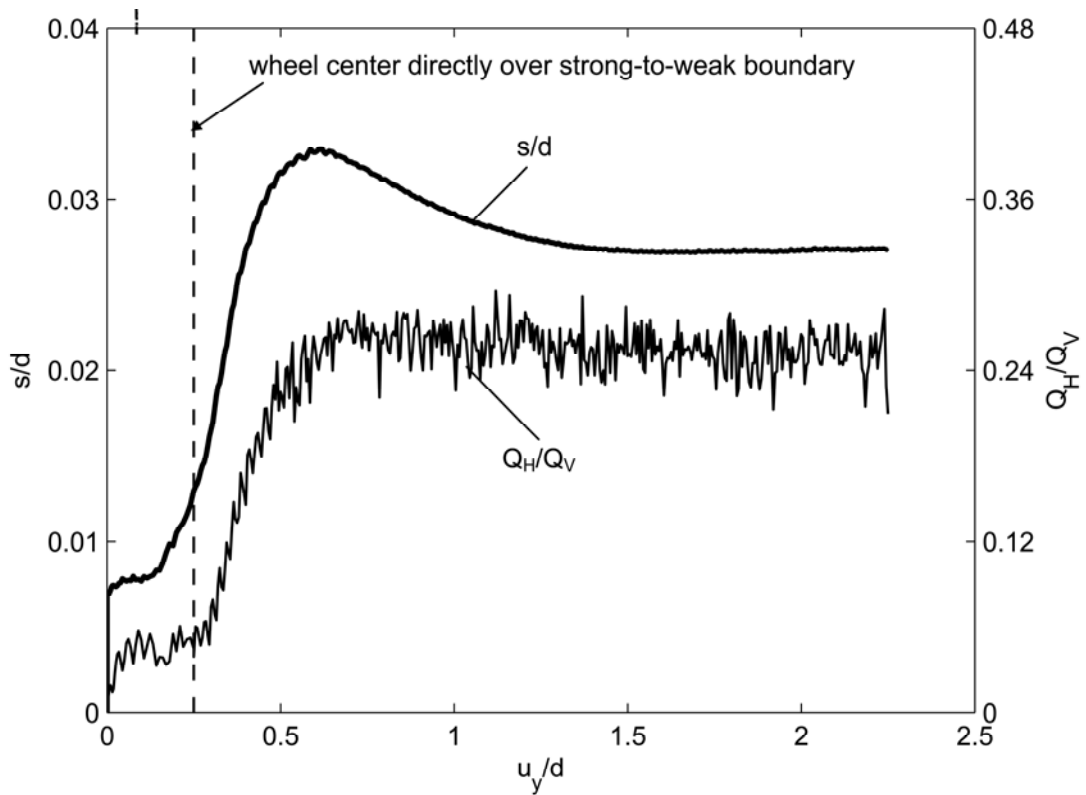


Fig. 4. Sinkage and horizontal wheel force vs horizontal wheel displacement for simulation with cohesive soil ($\varphi = \psi = 0$, $c/\gamma d = 1.25$, $b/d = 0.3$, $Q_V/\gamma b d^2 = 1.9$).

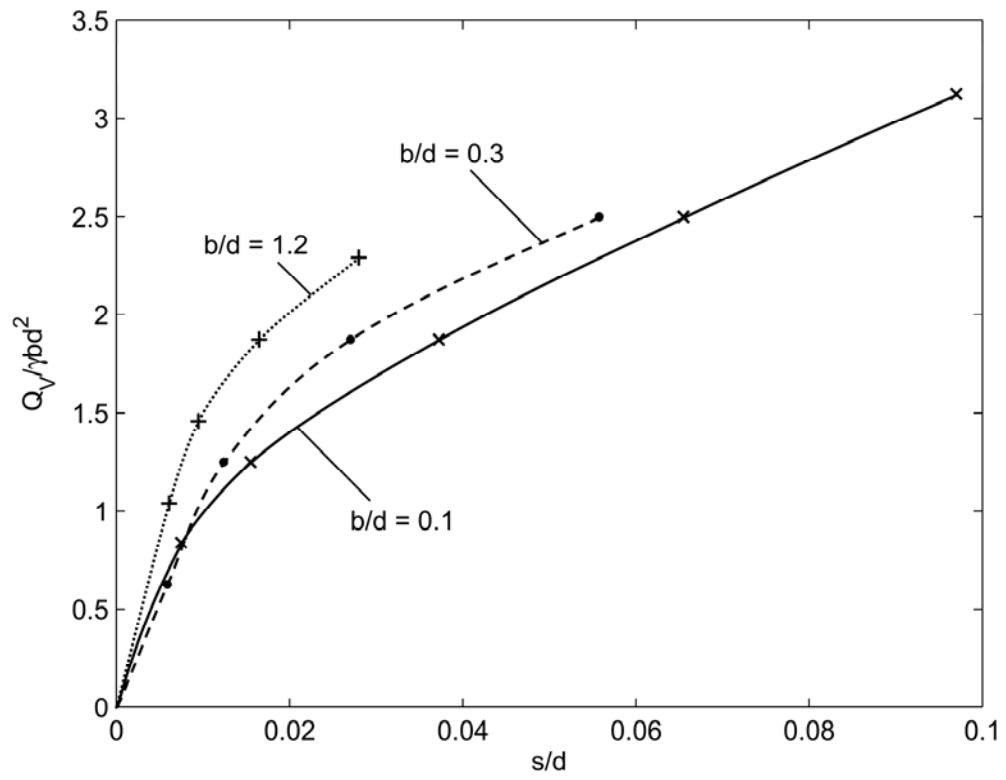


Fig. 5. Vertical force vs steady-state sinkage with varying wheel aspect ratios and cohesive soil ($\phi = \psi = 0, c/\gamma d = 1.25$).

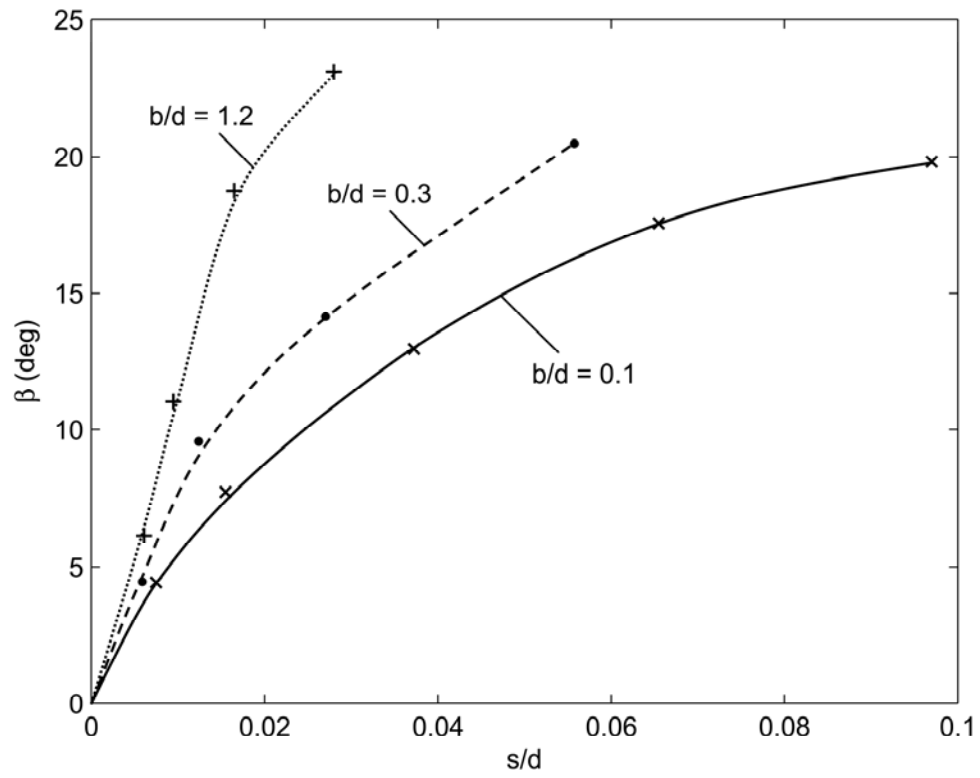


Fig. 6. Force inclination angle vs sinkage in steady state with varying wheel aspect ratios and cohesive soil ($\phi = \psi = 0, c/\gamma d = 1.25$).

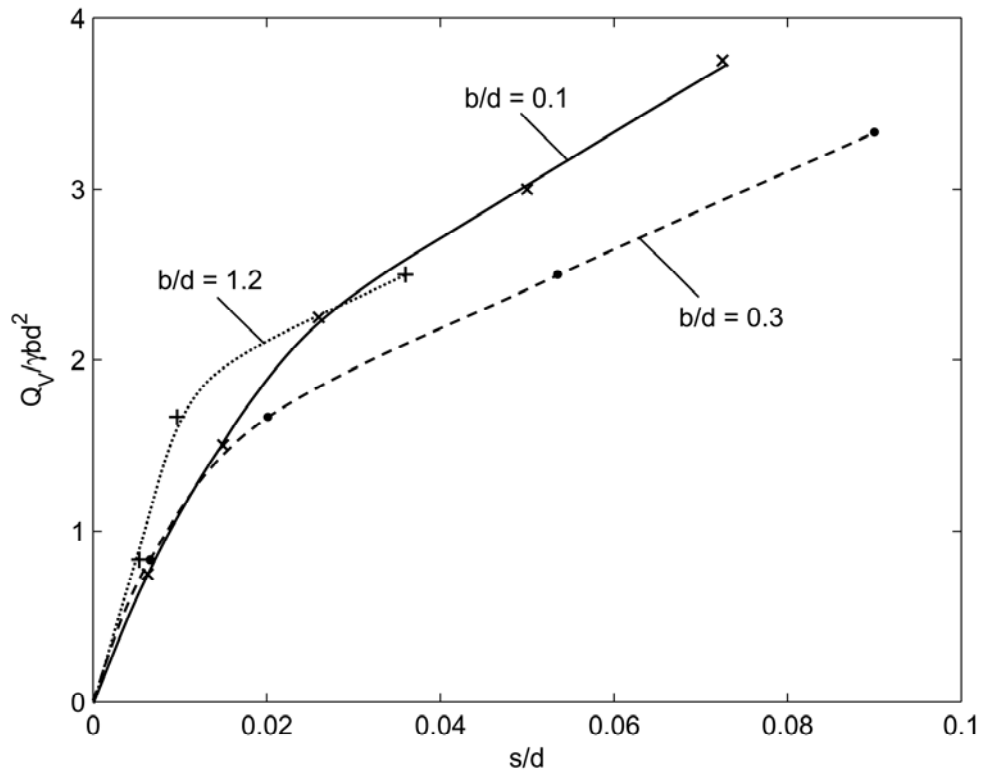


Fig. 7. Vertical force vs steady-state sinkage with varying wheel aspect ratios and frictional/cohesive soil ($\phi = 30^\circ$, $\psi = 0$, $c/\gamma d = 0.25$).

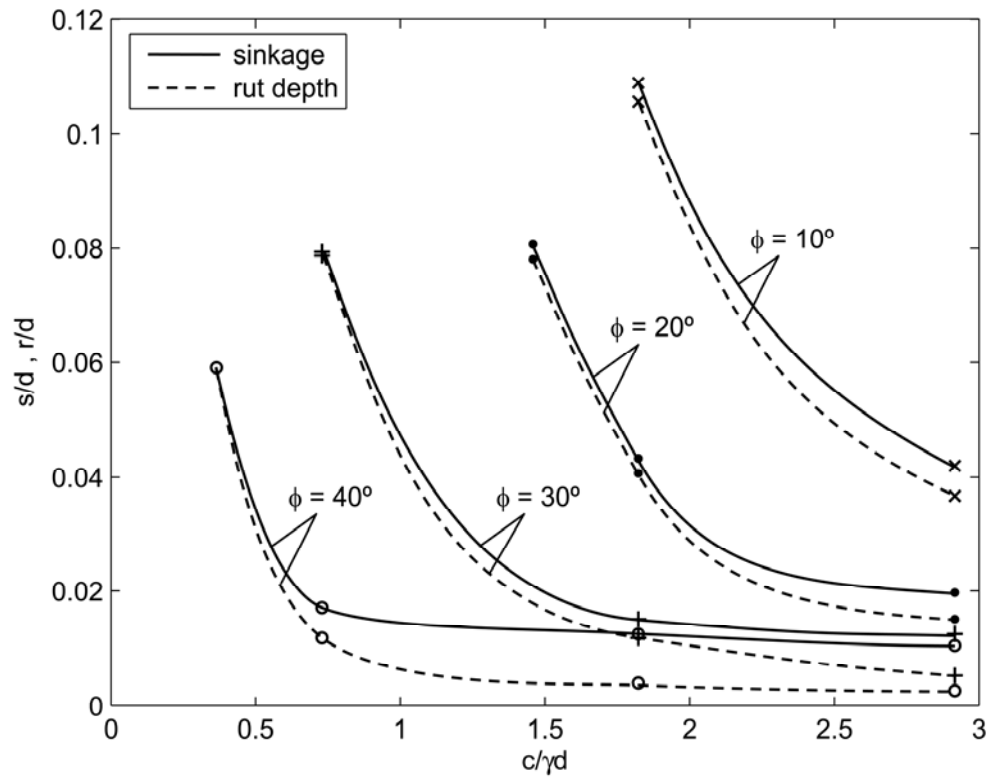


Fig. 8. Steady-state sinkage and rut depth from numerical simulations with varying soil properties ($Q_v/\gamma b d^2 = 7$, $b/d = 0.3$).

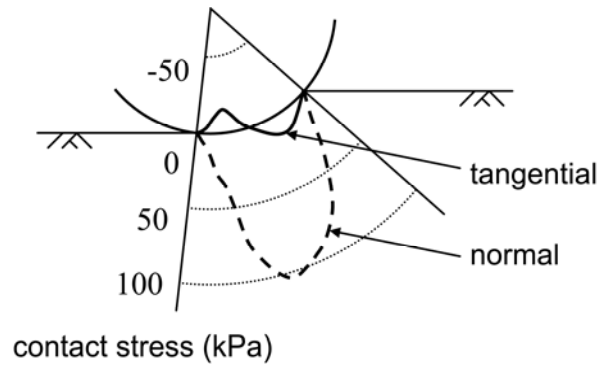


Fig. 9. Contact stresses measured by Onafeko and Reece [36] for towed rigid wheel with $d = 1.2$ m and $b = 0.3$ m on loose sand.

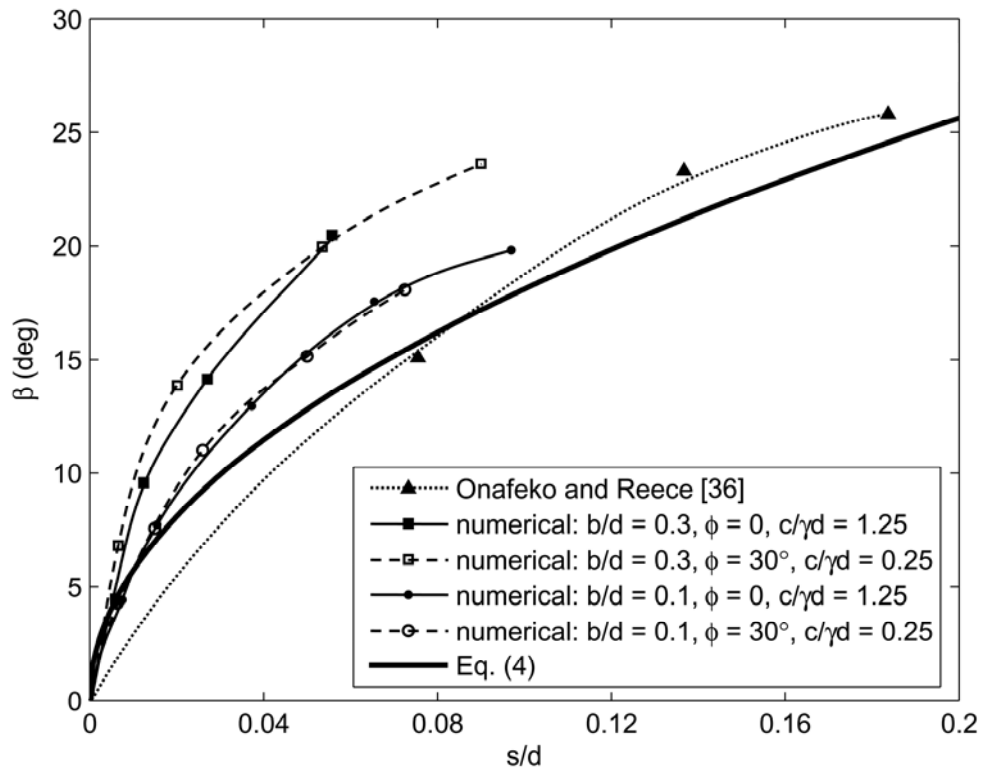


Fig. 10. Comparison of force inclination angle from Onafeko and Reece [36], numerical simulations (steady-state values), and Eq. (4).

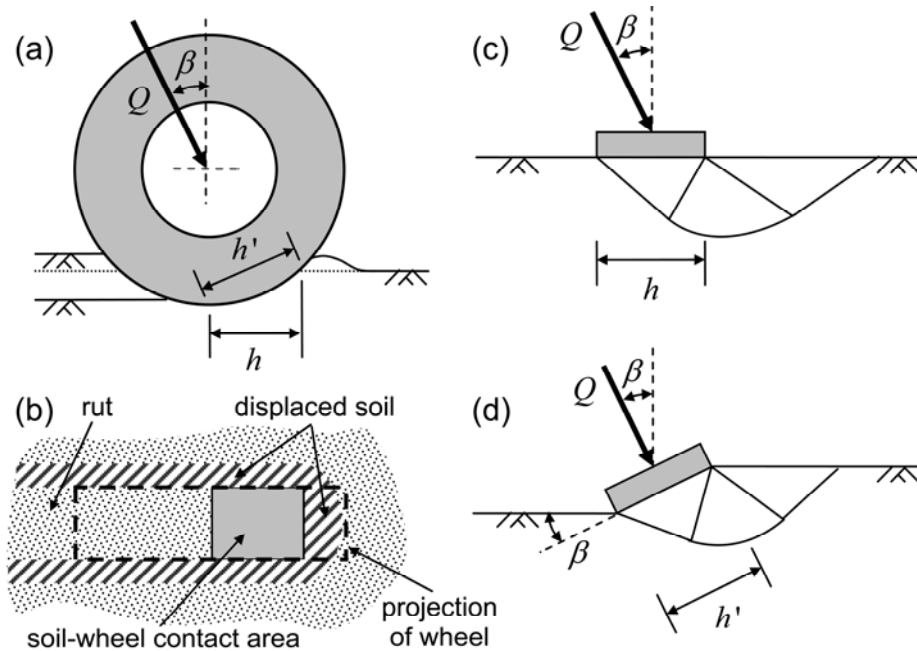


Fig. 11. Rolling wheel in steady state as analogous shallow footing: (a) side view of wheel; (b) plan view of wheel (direction of wheel travel is from left to right); (c) equivalent footing with inclined force; (d) equivalent inclined footing.

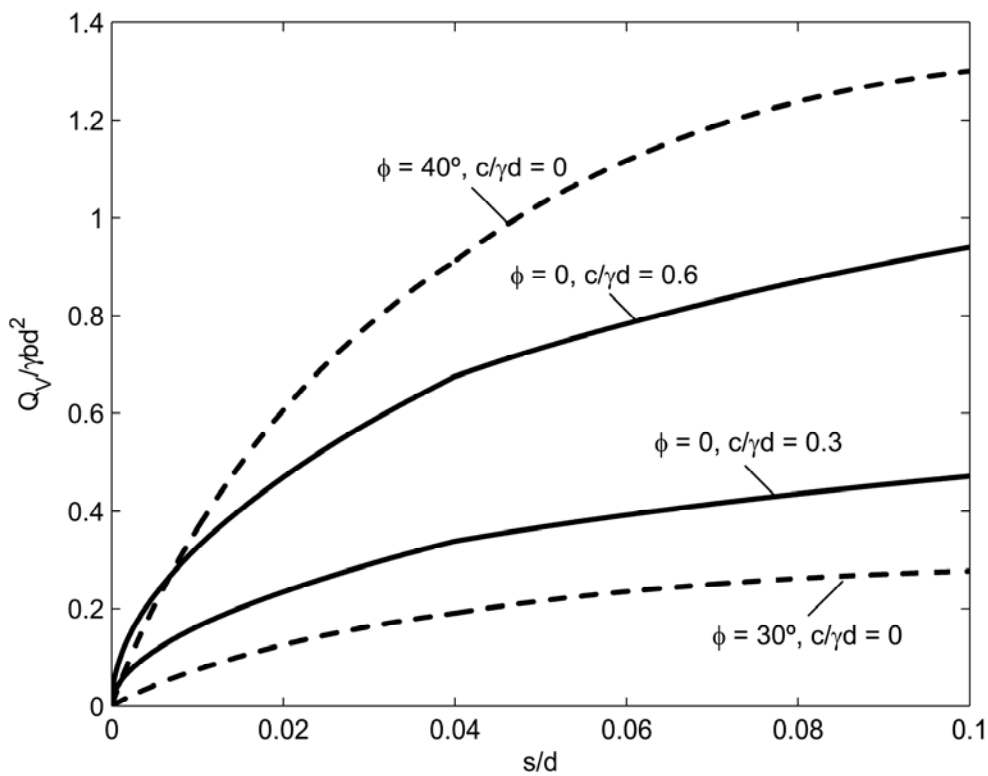


Fig. 12. Examples of vertical force vs sinkage using analytic (inclined footing) method with $b/d = 0.2$.

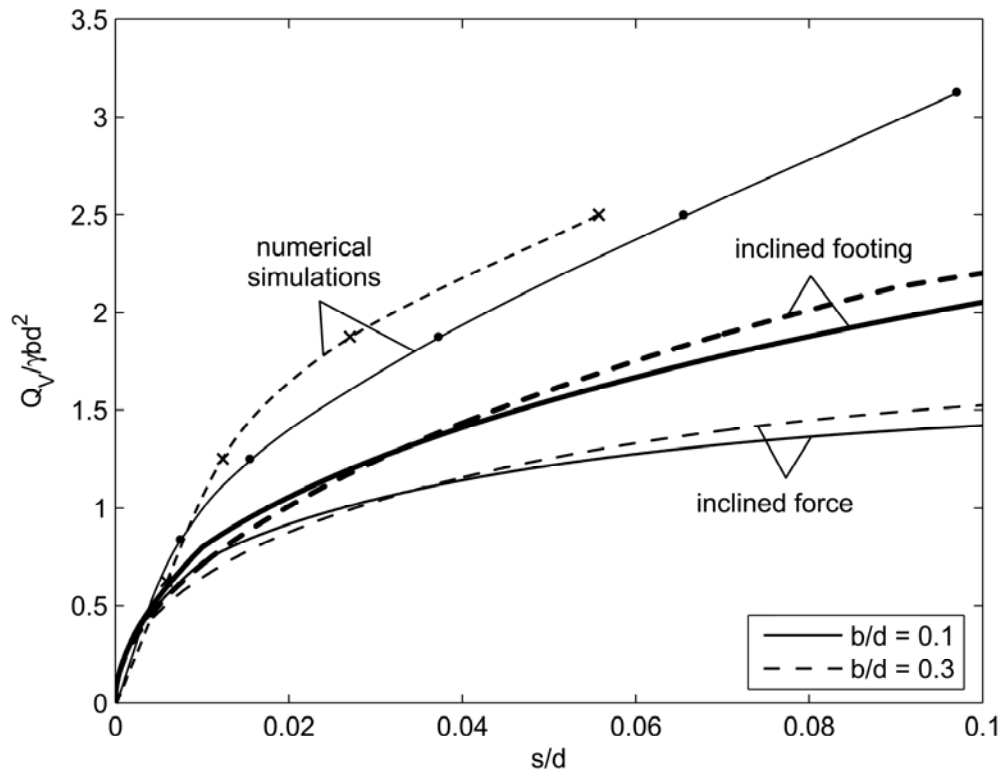


Fig. 13. Force-sinkage predictions using analytic method and numerical simulations with cohesive soil ($\varphi = \psi = 0$, $c/\gamma d = 1.25$).

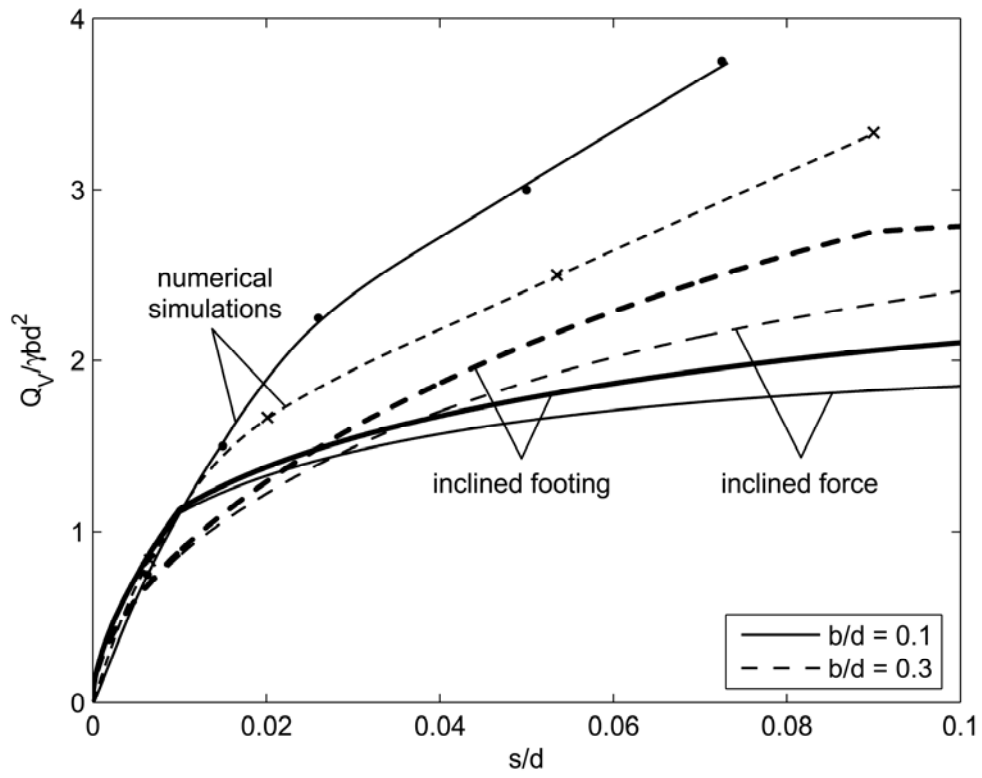


Fig. 14. Force-sinkage predictions using analytic method and numerical simulations with frictional/cohesive soil ($\varphi = 30^\circ$, $\psi = 0$, $c/\gamma d = 0.25$).

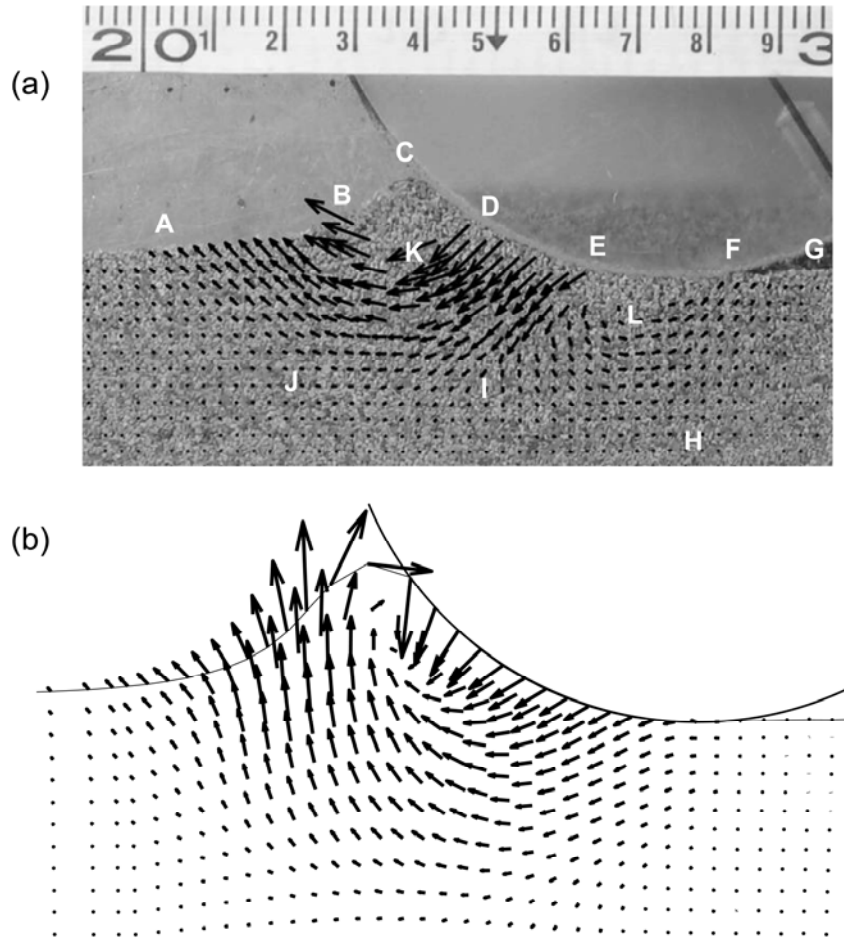


Fig. 15. Steady-state incremental displacement field in granular material approximating response at wheel midplane (direction of wheel travel is from right to left; numerals on scale denote cm): (a) experimental results using PIV; (b) results of numerical simulation ($\varphi = 40^\circ$, $\psi = 20^\circ$, $c/\gamma d = 20$).

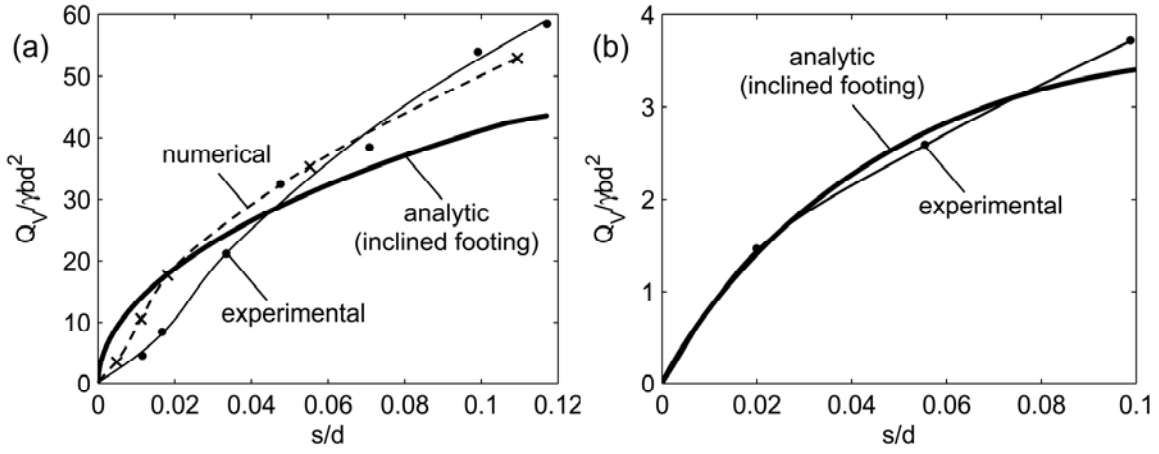


Fig. 16. Comparison of experimental and predicted steady-state force-sinkage curves: (a) clay ; (b) dense sand.

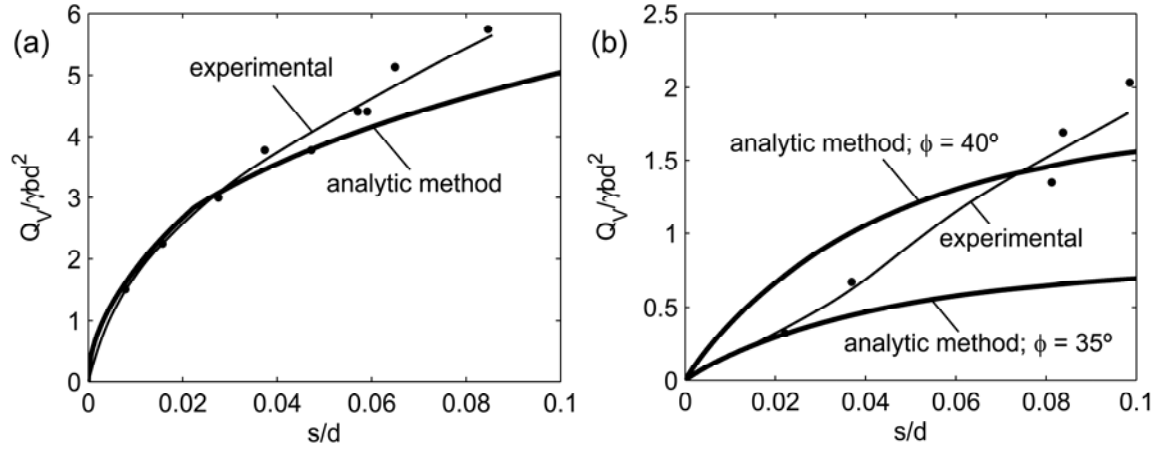


Fig. 17. Comparison of force-sinkage predictions using analytic (inclined footing) method and data from Willis et al. [47]: (a) clay; (b) sand.

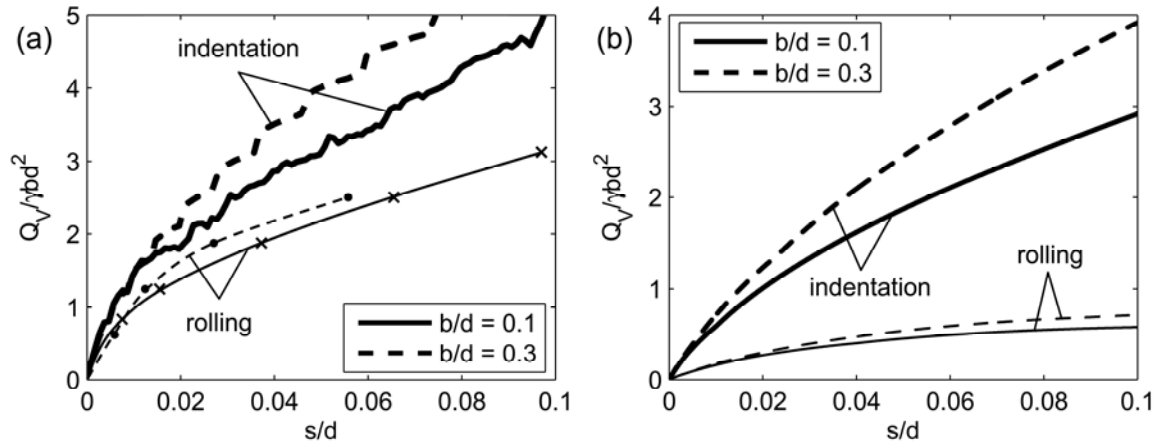


Fig. 18. Comparison of force-sinkage curves for steady rolling and indentation [3]: (a) results from numerical simulation with cohesive soil ($\phi = \psi = 0, c/\gamma d = 1.25$); (b) results from analytic method with frictional soil ($\phi = 35^\circ, c/\gamma d = 0$, inclined footing method).

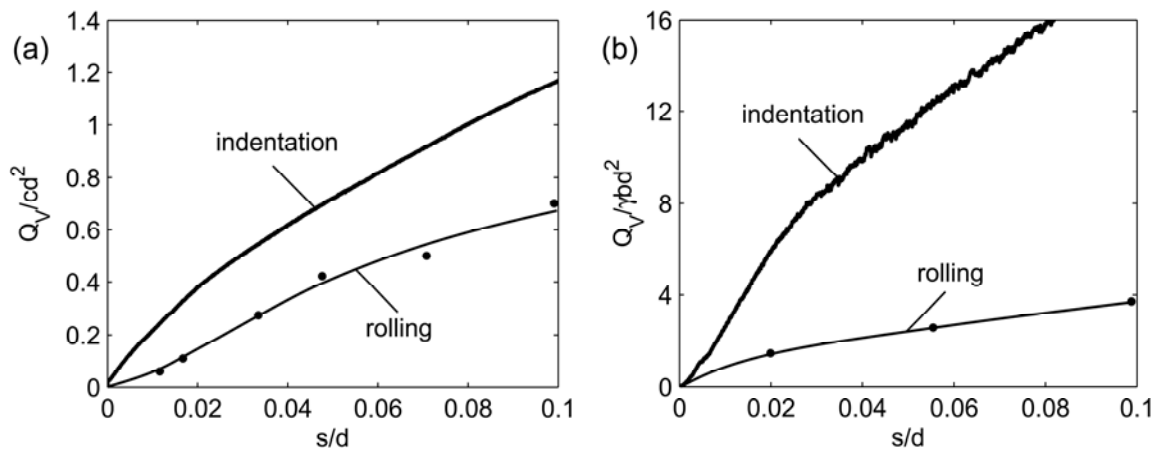


Fig. 19. Comparison of force-sinkage curves for steady rolling and indentation [3] from small-scale experiments: (a) clay; (b) dense sand.